J Opt
https://doi.org/10.1007/s12596-024-02177-2

RESEARCH ARTICLE

Integrated optic microring resonator for various sensing applications: design and analysis

Rishitej Chaparala[1,2] · Venkateswara Rao Kolli[3] · Srinivas Talabattula[4] · Sreenivasulu Tupakula[1,2]

Received: 1 June 2024 / Accepted: 17 August 2024
© The Author(s), under exclusive licence to The Optical Society of India 2024

Abstract A novel integrated optic microring resonator (MR) and MR based force sensor is reported. The micro-ring's and bus waveguide's width, and coupling gap of MR are optimized using Finite-Difference-Time-Domain (FDTD) Method. This optimized MR provides large FSR and high Q-factor. The optimized IOMR is used as an optical sensing element in force sensor. MR is integrated into the micro cantilever beam (MCB) of the force sensors. The radius and thickness of MR are considered as 5 µm radius and 220 nm respectively, and length, width and thickness of MCB is considered as 75 µm, 15 µm and 300 nm respectively. The working principle behind the sensor is principle of photo-elastic effect. The effective refractive index of the sensor changes when a force is applied to the sensing element, which leads to a resonant wavelength shift of MR output characteristics. A shift in resonant wavelength is detected as a function of the applied force. The Finite-Element Method is used to analyze the sensor's stress, and the FDTD method is used to analyze MR's field propagation. The optimized MR provides an FSR of 22.29 nm. The sensitivity of the force sensor is 5 pm per 1µN and Q-factor is 18,241. The sensor range is from 0 to 1 µN. The optimized MR can be used for different sensing applications such as force, pressure, acceleration sensing, biosensing, etc.

Keywords Microring resonator · Finite element method · Microcantilever beam · Q factor · Force sensor · Full width half maximum · Free spectral range · Low force

Introduction

Micro-Electro-Mechanical Systems (MEMS) are lightweight and compact, making them ideal for measuring pressure, force, acceleration, and temperature in aerospace, biomedical, automotive industries, etc [1]. MEMS sensors available in the market based on different detection methods, especially, interferometry [2], tunneling [3], piezoelectric [4], piezoresistive [5], interdigital [6], capacitive [7], etc.

Compared to MEMS, integrated optic (IO) MEMS, also known as IOMEMS, are simpler, less expensive, and highly sensitive. They are used in electro-magnetically active systems, and ultra-high vacuum systems. A new technology called silicon-on-insulator (SOI) allows the fabrication of IOMEMS components with core sizes smaller than micrometers, and sharp bends with radii of less than a few micrometers [8–12].

IO ring resonators with small sizes are a major factor in the rapid development of success of silicon photonics. The compact design, high optical field enhancement within cavities, good wavelength selectivity and high Q-factor etc, are some of the benefits of ring resonators. Numerous uses for these special qualities in optical passive and active systems have been proven. MR are essential elements in various applications especially, communication systems, quantum applications, etc [13–15]. The researchers have reported the high quality miniaturized micro-cavity resonators for various communication applications especially wavelength add-drop filters in wavelength-division- multiplexing systems [16, 17], switching, routing systems and modulation [18, 19],

✉ Venkateswara Rao Kolli
venkukolli@gmail.com

1 Electronics and Communication Engineering, SRM University, Mangalagiri, AP 522502, India

2 Centre of Excellence for Electronic Cooling, SRM University, Mangalagiri, AP 522502, India

3 Electronics and Communication Engineering, Malnad College of Engineering, Hassan 573202, India

4 Electrical Communication Engineering, Indian Institute of Science, Bangalore, India

Published online: 31 August 2024

group-delay [20], add-drop filters [21, 22], signal processing [23, 24], laser systems [25, 26], Raman lasers [27], etc.

Ring resonators' positions and shapes are extremely sensitive to a variety of effects [28], including magneto-optic, electro-optic, photo-optic, acoustic-optic, nonlinear-optic, magneto-optic effects, and electro-absorption which will lead to changes in the resonant wavelength [29], etc. Several IO ring resonator based devices for sensing applications in Label-free bio sensors [30], glucose sensing and seismic sensing, Trinitrotoluene sensing [31], biochemical sensors [32–34], accelerometers [35–38], etc were reported. A racetrack based accelerometer sensor of frequency less than 200 Hz that is highly sensitive, immune to electromagnetic interference, and lightweight has been demonstrated [39]. A vibration sensor based on a MOEMS racetrack resonator (RTR) has been reported, The sensor exhibits a sensitivity of 3.19 pm/g [40]. A RTR sensor using SOI technology has been reported [41]. An optical sensor with a sensitivity of 430 nm/RIU is reported [42]. A urea sensor with a 7×10^{-3} nm spectrum shift, based on racetrack resonators, has been described [43]. The force sensor using GaAs-Al0.6Ga0 as platform [44, 45] The atomic force microscopy has been reported [46, 47] A force-sensor based on IOMEMS RTR has been published, featuring Q of 8153 [48]. A coupled IOMR force sensor of high Q-factor of 19,000 is reported [49]. IO serially coupled RTR pressure sensor with a sensitivity of 1.04 nm per 100 kPa is reported [50]

In the current literature, it is observed from the most of the work that the dimensions of microring and input and output waveguides widths are equal (example: either 450 nm or 500 nm etc.). But in this work, the width of input and output waveguides is identified as 450 nm and the width of microring waveguide is identified as 500 nm. This is a novel idea. But while comparing the other force sensors, the force sensor reported is novel integrated optical MR based force sensor provides very high Q-factor of 18241.

In this work, the force sensor consists of a mechanical cantilever beam (MCB) and MR. MR of radius 5 µm is optimized for high intensity and high quality factor (Q-factor) by the FDTD-Method. An optimized MR is considered as sensing element in the force sensor. MR is integrated into mechanical MCB. The analysis of the sensor is done by two methods. Here, the stress of MCB is analysed by FEM and the FDTD is used to analyze the electromagnetic filed propagation through the MR. There is a change in the effective refractive index (ERI) of MR for appled force, which results in shift of resonant wavelength at MR's transmission port. This is due to photo-elastic effect and optomechanical coupling. This shift can be measured as an applied force. The high Q-factor of 18,241 is achieved at the MR's coupling-gap of 200 nm. This sensor provides a sensitivity of 5 pm per 1 µN and a Free Spectral Range (FSR) of 22.29 nm.

Analysis of microring resonator

An optical ring-resonator in its general form is made up of a waveguide that is self-looping. When a ring's optical path length is precisely a whole number of wavelengths, resonance occurs.

All pass microring resonator

IO Microring Resonator (MR) consists of a microring coupled to straight waveguides (input/output ports). These waveguides are used to input and output light. MR is mainly in two configurations, an all-pass MR consists of microring of radius R with a single bus waveguide as depicted in Fig. 1a. Figure 1b depicts add-drop MR. It is similar to all-pass MR with an added second bus waveguide. The input field is coupled to a microring by a bus waveguide.

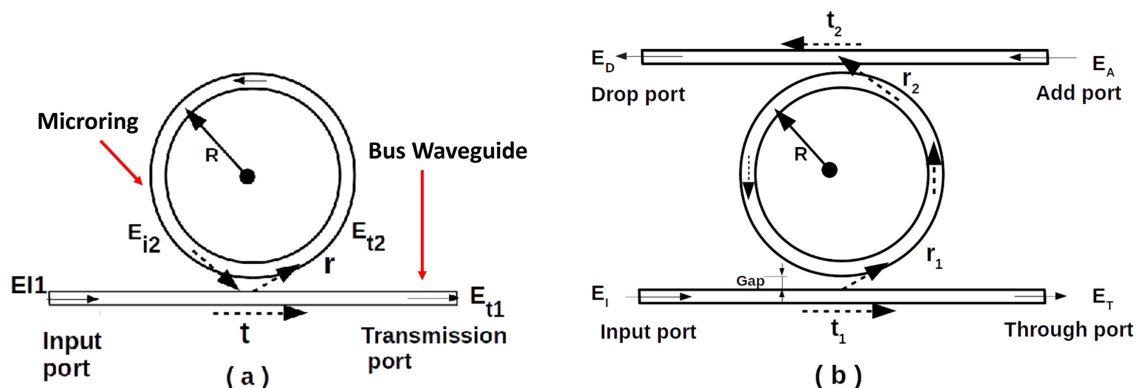

Fig. 1 Schematic diagrams of **a** All-Pass and **b** Add-Drop microring resonator

$$\lambda_{res} = \frac{n_{eff}L}{m} \quad where \quad m = 1, 2, 3, \ldots \tag{1}$$

where $L = 2\pi R$, is a circumference of microring, R is radius, n_{eff} is ERI of the waveguide.

The field relations between input and output fields are analyzed as follows. When the wave E_{i1} is applied at the input-port, the output waves in terms of incoming waves are given by [51]

$$E_{t1} = tE_{i1} + irE_{i2} \tag{2}$$

$$E_{t2} = tE_{i2} + irE_{i1} \tag{3}$$

The traveling waves circulating in microring are given as

$$E_{i2} = E_{t2}e^{-(\alpha L + i\phi)} \tag{4}$$

where α is the propagation loss coefficient, ϕ is the phase constant, t is transmission coefficient, r is coupling coefficient.

The relation between two coefficients is:$t^2 + r^2 = 1$. The power intensity at transmission-port in terms of initial field E_{i1} is given by [49, 51]

$$I_t = \left|E_{t1}\right|^2 = \left|\frac{t - e^{-(\alpha L + i\phi)}}{1 - t\left(e^{-(\alpha L + i\phi)}\right)}E_{i1}\right|^2 \tag{5}$$

Field Enhancement (FE): It is ratio of wave circulating inside the microring to that of input wave and is given by

$$FE = \frac{r}{1 - t(e^{-\alpha L})} \tag{6}$$

FE is an essential factor, which indicates the field intensity buildup in microring for the applied field at the input-port. High transmission coefficient and small coupling coefficient provides maximum FE.

Figure 2 shows the FWHM graphical representation.

FSR: It is a frequency spacing between two subsequent resonances and gives the usable range of wavelengths for communication and sensing applications. SOI is a high refractive index material with core, cladding, and substrate. Hence, by considering the group refractive index n_g [51, 52].

FSR is

$$FSR = \frac{\lambda^2}{n_g L} \tag{7}$$

where

$$n_g = n_{eff} - \lambda\frac{\partial n_{eff}}{\partial \lambda} \tag{8}$$

The remaining characteristics are represented by assuming a loss term as follows

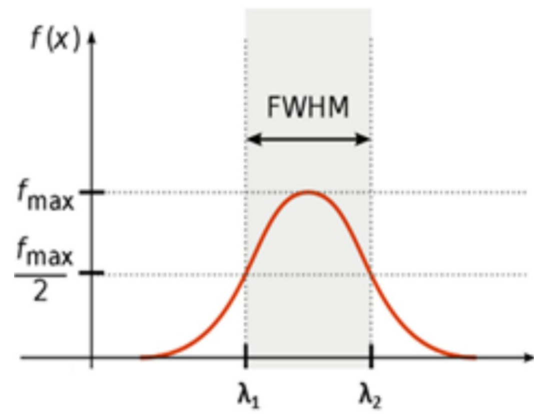

Fig. 2 FWHM graphical representation

$$\chi = e^{-\alpha L} \tag{9}$$

Full-Width-Half-Maximum (FWHM): FWHM of a resonance spectrum is given by

$$FWHM = \frac{(1 - t\chi)\lambda_{res}^2}{\pi n_g L\sqrt{t\chi}} \tag{10}$$

Figures 3a and b show the effect of radius (R) and group refractive index (n_g) on FWHM. It is observed from Fig. 3a that a smaller radius provides higher FWHM. Also, Fig. 3b shows the effect of n_g on FWHM,it is observed that higher n_g provides low FWHH. The narrow FWHM provides a high Q-factor, which is a desirable characteristic for sensing applications. Figure 3c represents the effect of radius on the FSR. Since it is inversely proportional to the FSR, it is a high at low radius but it decreases as the radius is increased. The effect of n_g on FSR is as shown in the Fig. 3dd. Compared to n_g, the effect of the radius is higher on FWHM and FSR.

Finesse shows the resolving power of the MR as a filter [51].

The Q-factor's reliance on coupling coefficient and operating wavelength are as shown in Fig. 4a and b. It is observed that high radius and lower coupling coefficient provides higher Q-factor. Figure 4c and d show the dependency of finesse on loss factor, transmission coefficient, and coupling coefficient. When loss factor is 1 the finesse is more and also at low coupling coefficient, finesse is higher. Finesse is represented as follows

$$Finesse = \frac{FSR}{FWHM} \tag{11}$$

The Q-factor: It is the ratio of stored energy to power lost in one optical cycle [51, 52].

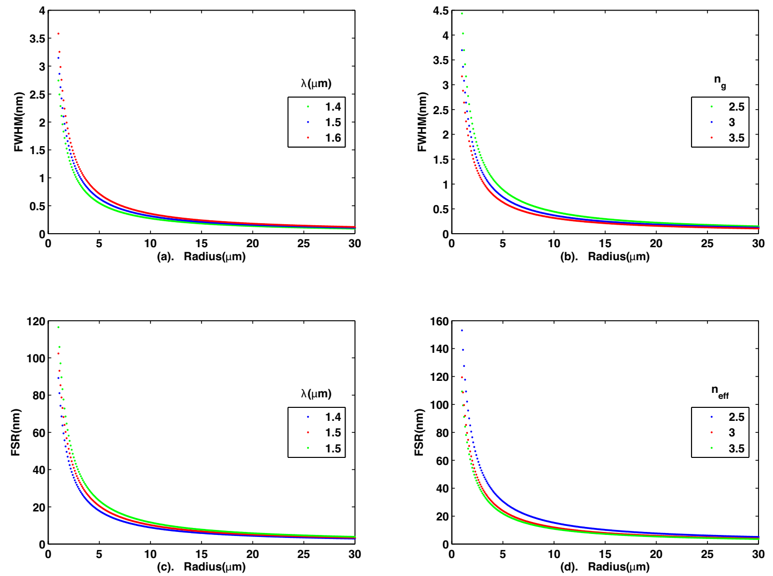

Fig. 3 Variation of FWHM and FSR with Radius of microring and other parameters

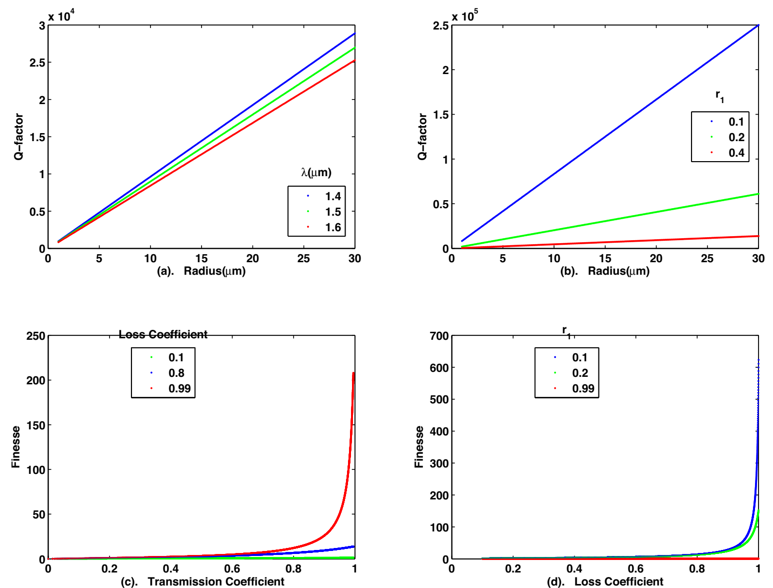

Fig. 4 Variation of the Q-factor and Finesse with coupling coefficient

$$Q = \frac{\lambda_{res}}{FWHM} \tag{12}$$

The finesse and Quality factor are expressed in terms of physical parameters as follows

$$Finesse = \frac{\pi\sqrt{t\chi}}{1 - t\chi} \tag{13}$$

$$Q = \frac{\pi n_g L \sqrt{t\chi}}{\lambda_{res}(1 - t\chi)} \tag{14}$$

The high sensitivity and Q-factor are desirable parameters for sensing applications. In general, miniaturized MR are devices are advantageous, but less radius leads to more bending losses and reduced Q-factor. But increasing the coupling-gap of MR increases the Q-factor of MR. Any changes in circumference of microring and or ERI of any waveguide of MR or any waveguide of an IO sensing element shifts the resonance wavelength of transmission spectrum at the output port of the sensor and this shift is proportional to an applied force, pressure or any other physical parameters.

Design and analysis of MR

The design dimensions of MR are: radius is 5 μm, bus and microring waveguide width and thickness of bus are 500

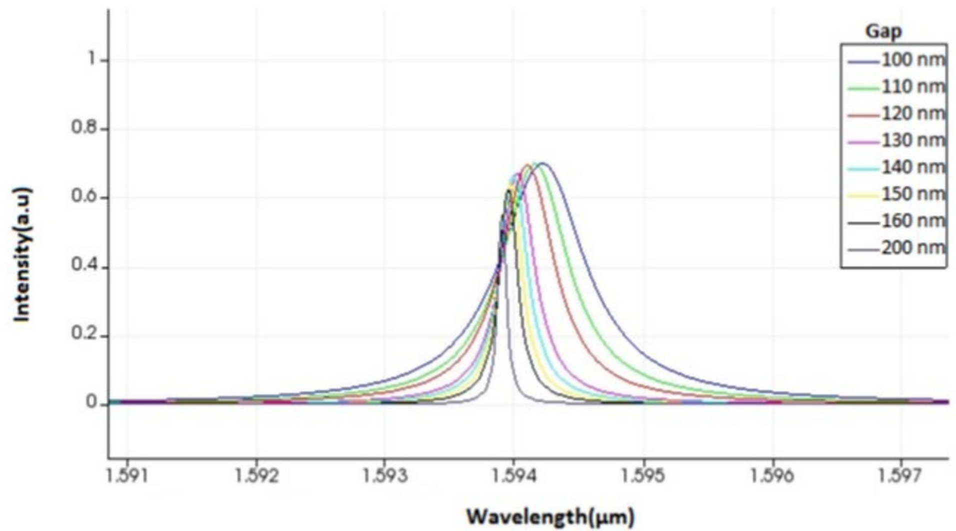

Fig. 5 E-Field intensity of MR at coupling-gap varied from 50 to 250 nm

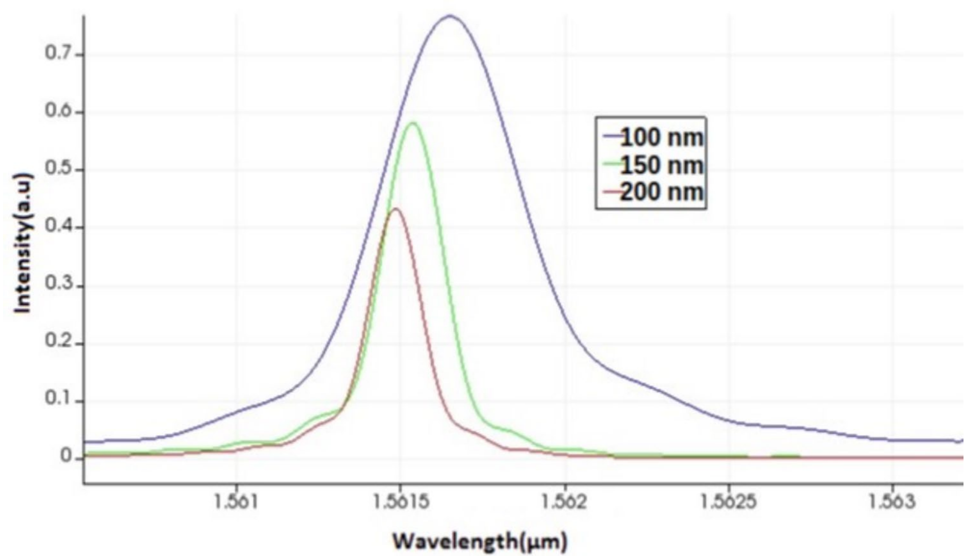

Fig. 6 Field intensity of MR at three coupling-gaps

nm and 220 nm respectively [50, 52]. The dimensions of IO device waveguide is around thickness of 220 nm and width of 500 nm for single mode operation [53, 54]

Table 1 Comparison of intensity, FWHM and Q-factor at different gaps

Gap (nm)	FWHM (nm)	Q-factor
100	0.63	2570
150	0.25	6470
200	0.09	18,241

Varying coupling-gap of MR

The microring and bus waveguide widths are maintained at 500 nm, but the coupling-gap between them is adjusted between 100 nm and 250 nm, to optimize MR. Figure 5 illustrates how the field intensity varies for different coupling-gaps at the transmission port. Figure 6 shows the same for 100 nm, 150 nm, and 200 nm gaps [52].

It is observed from Table 1 that MR with low coupling-gaps (i.e., 100 nm) provides high-intensity, and large-FWHM (large -FWHM produces low-Q). When the gap is large (i.e., 200 nm), intensity is lower but the Q-factor rises to an extremely high value (at Gap of 200 nm, the Q-factor is 18,241). In this force sensor, high Q-factor high-intensity, and low-FWHM are considered. These characteristics are obtained when MR is at the gap of 150 nm.

It is evident from Figs. 5, 6 and Table 1 that an increase in coupling-gaps causes an increased Q factor and alters intensity and shift in resonant wavelength. Equation 17 explains

effect of coupling coefficient, which in turn affects the Q-factor. And also effects the intensity at transmission port and shift in resonant wavelength(as shown in Fig. 5). This characteristic has applications in sensing. This analysis concludes that MR with a coupling-gap of 150 nm offers a high Q-factor of 6470 and a low-FWHM of 0.25. Hence, optimized coupling gap of MR is considered as 150 nm. And, any changes in coupling-gap by external physical parameters will change the resonant wavelength of MR. And any external physical parameter can be read out in terms of resonant wavelength shift. This phenomenon can be exploited in sensing applications.

Varying microring width of MR

Microring width is optimized by varying it between 400 and 700 nm while maintaining the bus waveguide width at 500 nm, and coupling-gap at 150 nm. The field profile of MRs for various microring widths, ranging from 400 nm to 700 nm, is shown in Fig. 7. Figure 7 illustrates how MRs with microring widths between 500 and 600 nm can produce E-field profiles that have a single mode profile [52]. A high Q-factor of 13,418 is achieved by MR with a microring width of 650 nm. A microring width of 650 nm results provides high Q-factor of 13,418. These are significant findings.

Figure 7 and Table 2 shows that an increase in microring width to 650 nm is accompanied with a rise in the Q-factor of 13418. However, as Fig. 7 illustrates, MR's E-field profile changes into side modes or double modes over 550 nm of microring width. Therefore, 500 nm is thought to be an ideal microring width which will give high-intensity and high Q-factor. After taking these benefits and drawbacks into account.

Table 2 The Q-factor and FWHM of MR at different microring widths

Microring width (nm)	FWHM (nm)	Q-factor
450	0.24	6758
500	0.22	7352
550	0.18	8941
600	0.18	8941
650	0.12	13,419

Figure 8 shows transmission spectra of MR at different microring widths. It is identified from Fig. 8 that when microring width is varied, resonant wavelength of transmission spectra of MR is shifted. It shows that any changes in microring width by external physical parameters will change the resonant wavelength of MR. This is also an important finding. Hence, changing the microring width by external physical parameters (temperature, force, pressure, etc) is proportional to a shift in resonant wavelength of MR. This effect can be applied to sensing applications.

Varying bus waveguide width of MR

Initially, to optimize bus waveguide width, it is changed from 400 nm to 700 nm by keeping the microring width and coupling-gap at 500 nm and 150 nm respectively. Figure 9 shows, E-field profile of MR for various width of bus waveguide. It is observed from Fig. 9 and Table 3 that MR with 450 nm bus waveguide width gives high-intensity, high Q factor and low-FWHM [52].

The transmission characteristics of MR at various bus waveguide width is as shown in Fig. 10. It is observed from Fig. 9 that when there is a change in bus waveguide

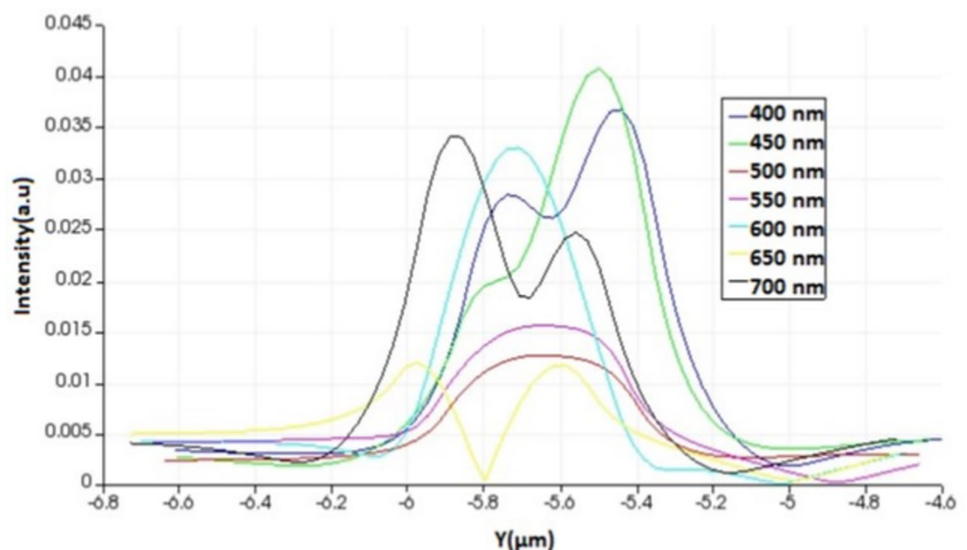

Fig. 7 E-field profiles of MR for different microring widths

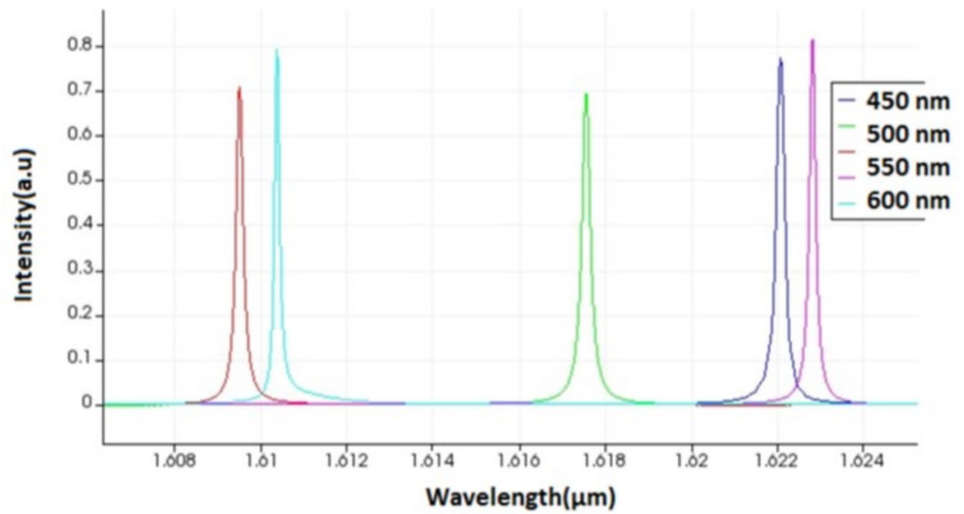

Fig. 8 Transmission characteristics of MR with different microrg widths

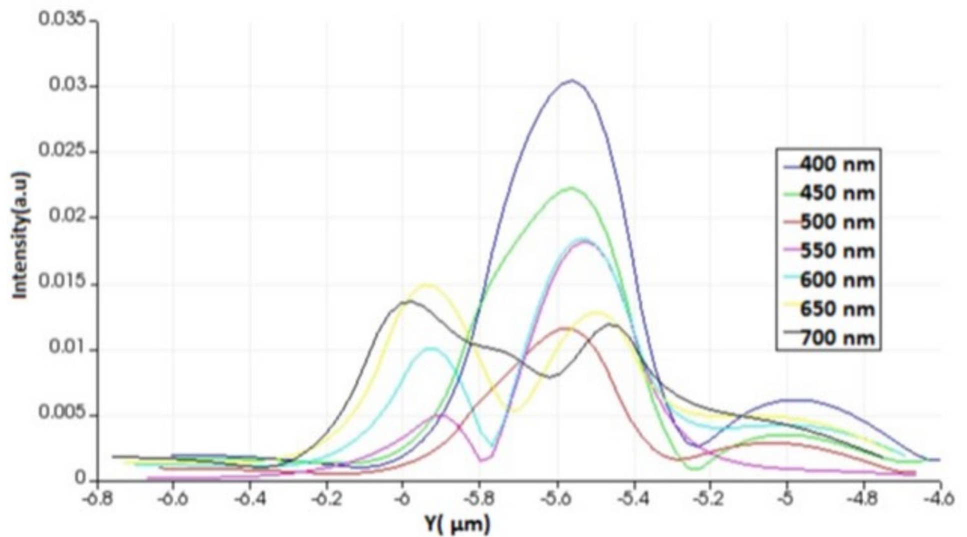

Fig. 9 E-field profile at the transmission port for varying bus waveguide widths

Table 3 Q-factor and FWHM with different bus widths

Bus waveguide width (nm)	FWHM (nm)	Q-factor
400	0.30	5312
450	0.21	7590
500	0.23	6930
550	0.29	5498
600	0.37	4308

width, there is a resonant wavelength shift at output spectra of MR. And, any changes in microring width by external physical parameters will change the resonant wavelength of MR. Hence, any change in bus waveguide width by external physical parameter can be expressed as a change in resonant wavelength of MR. This effect also can be used in sensing applications.

Optimized 5 µm radius MR

Figure 11 shows the field intensity of MR at non-resonant and resonant conditions of MR. When MR is in resonance, maximum field couples to the microring and finally to the transmission port as depicted in Fig. 11b. On the other hand, in case of MR is in non resonance, a fraction of the E-field will be coupled to microring, but most of the field transfers to the transmission port as shown in Fig. 11a.

Finally, the optimized parameters obtained in previous sections are used to model an optimized MR. Further to validate these optimized parameters, the MR is analysed by keeping optimized gap of 150 nm and microring width and waveguide width of 500 nm and 450 nm respectively. The transmission characteristics are as shown in Fig. 12. An increased intensity, and the Q-factor of MR with 450 nm bus waveguide is because of high light confinement and

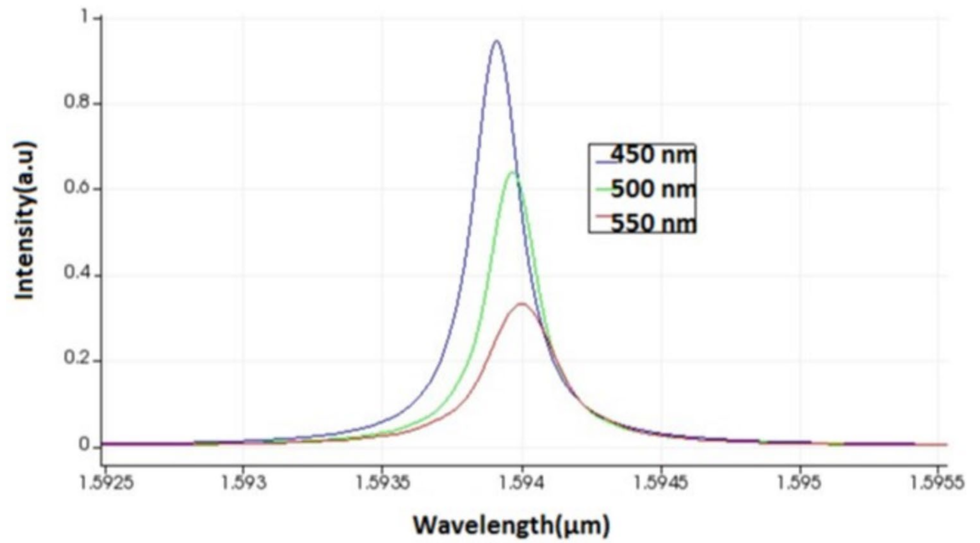

Fig. 10 Transmission characteristics of MR from 450 to 550 nm bus width

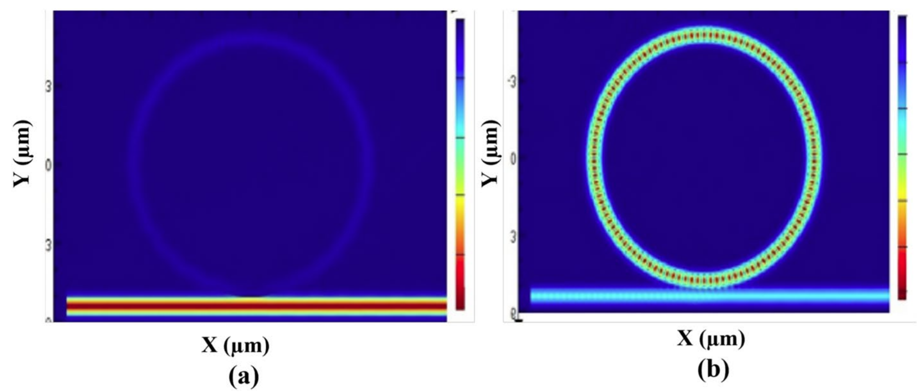

Fig. 11 MR characteristics at (**a**) Resonant and (**b**) Non resonant conditions

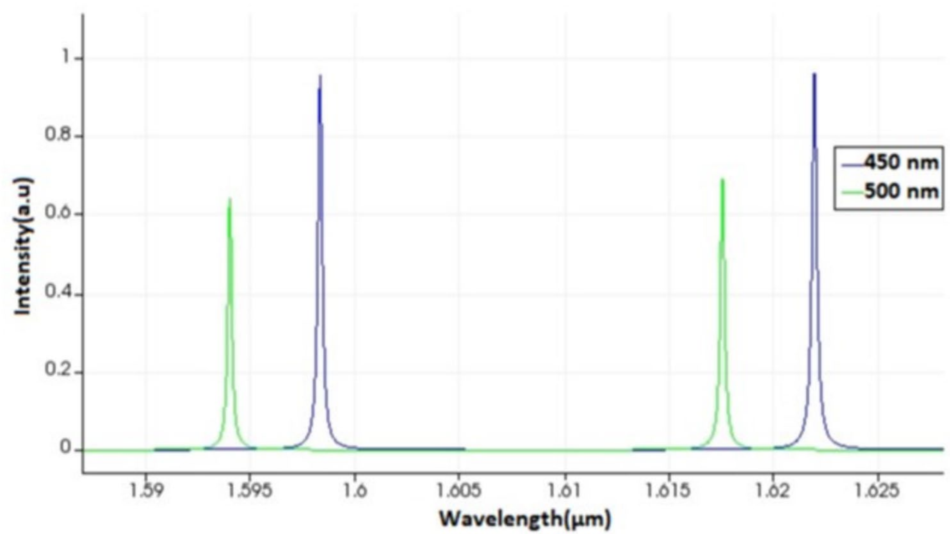

Fig. 12 Transmission characteristics of MR at 450 nm, and 500 nm bus waveguide widths

lower propagation losses compared to the other dimensions. MR with these optimized parameters provides high intensity, single mode E-field profile and high Q-factor of 7590 [52].

Figure 13 shows FSR of different microring resonators. It is observed from Fig. 13 that rings with larger radius provides less FSR as the radius and FSR are inversely

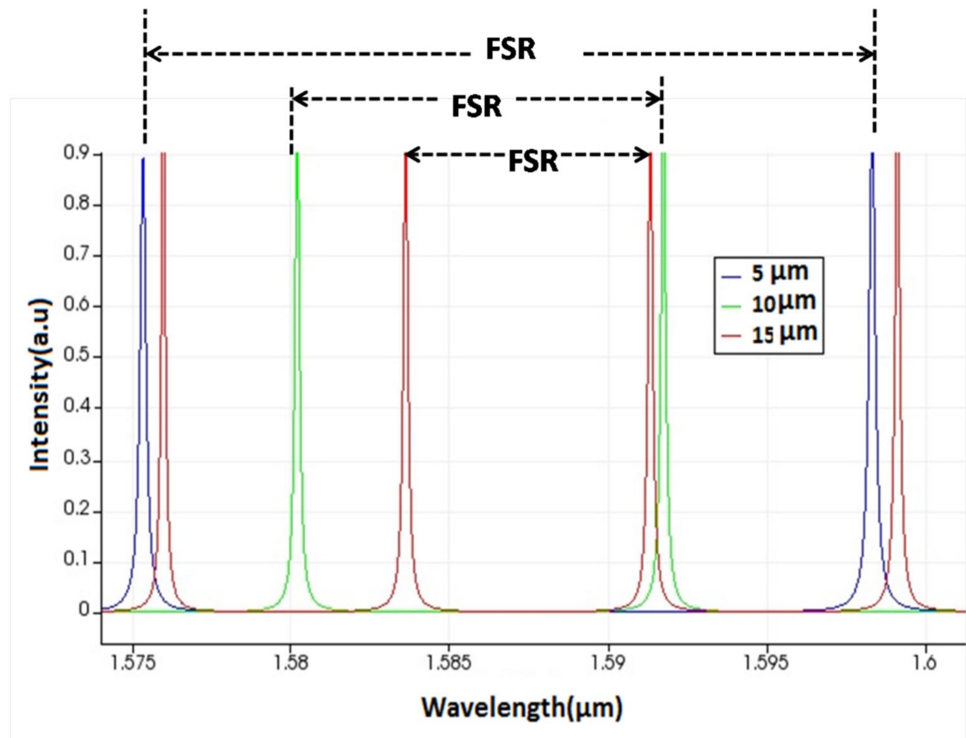

Fig. 13 FSR of three microrings with different radii

Table 4 Characteristics of different MRs

MR (µm)	FSR (nm)	FWHM (nm)	Quality factor
5	23.65	0.21	7096
10	11.70	0.19	8438
15	7.78	0.17	9452

proportional to each other. The advancements in fabrication fields of nano science have enabled us to fabricate compact MR 's of the radii less than few microns(less than 5 µm). Hence, the large FSR which covers hole the optical window is possible with MR. This feature has given the microring resonator a clear edge over other IO devices as a futuristic component in IO circuits.

The comparison of different rings is given in the Table 4 and it is observed that lesser radius of ring provides high FSR and low Q-factor. Higher radii rings provide low-FWHM and high Q-factor. This is because of radiation losses in the microring.

Mechanics of micro cantilever beam

Figure 14 shows the schematic of MCB. The design of MCB depends on the suitable material properties, basic properties, aspect ratio and thickness.

Basic properties used in applications of force sensing, accelerometer sensing, AFM systems, etc., are the resonating frequency (f_0) and spring constant (k). The spring constant "k" of MCB in terms of physical parameters and Young's modulus is given by

$$k = \frac{EWt^3}{4L^2} \tag{15}$$

where "E" is $Young's$ modulus, "L" is length, "t" is thickness "W" is width, of MCB [55].

The resonance frequency is given by

$$f_0 = \frac{1}{2\pi}\sqrt{\frac{k}{m}} \tag{16}$$

where "m" is the mass of beam ($m = \rho * L * W * t$), where ερε is the material density). In order to minimize the external effects, f_0 should be a few kHz [56]. Hence, the design of MCB is optimized to have the "f_0" of 32 kHz and the "k" of 0.0312 N/m.

Figure 15 shows the effect of length and thickness on "k" and "f_0". The "k" versus length with width of 30 µm at thickness of 0.3 µm and 1 µm are plotted in Fig. 15a and b respectively. Similarly, the variation of spring constant and natural frequency with respect to the variation of thickness while keeping the length at 50 µm, 100 µm and 200 µm are plotted in Fig. 15c and d. From figures, it is observed that thinner MCB provides lower spring constant. The mechanics of beams, bridges and diaphragms is generally given by [57]:

$$D(\omega) - c\frac{\partial\omega}{\partial t} - \rho h\frac{\partial^2\omega}{\partial h^2} = -q(t), \tag{17}$$

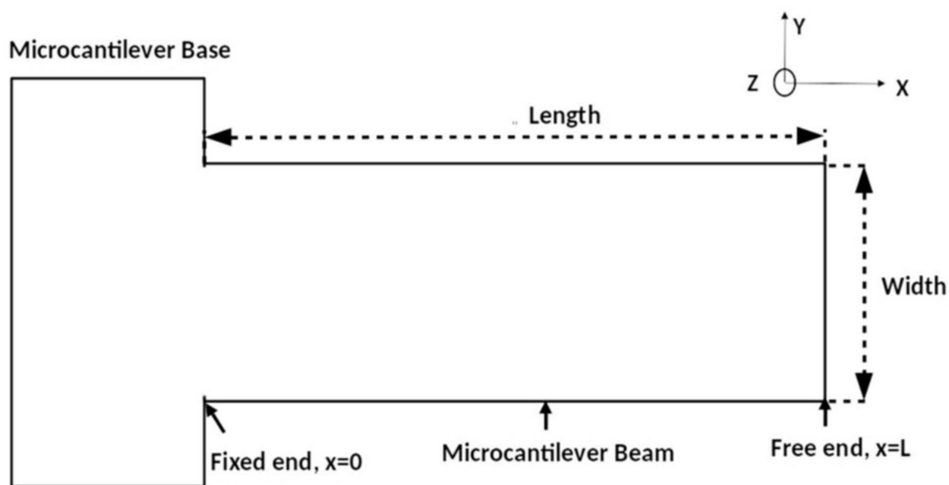

Fig. 14 Schematic of Microcantilever Beam

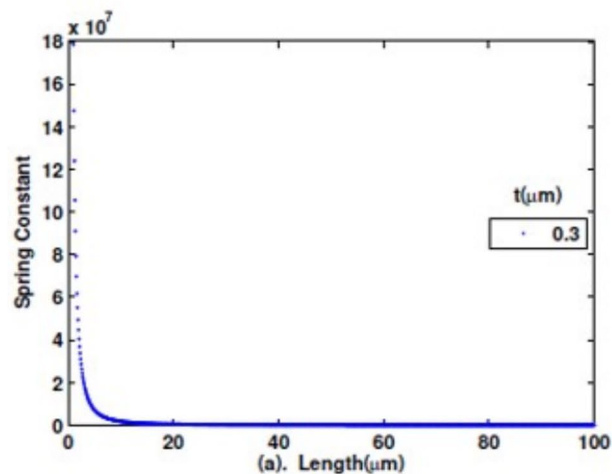

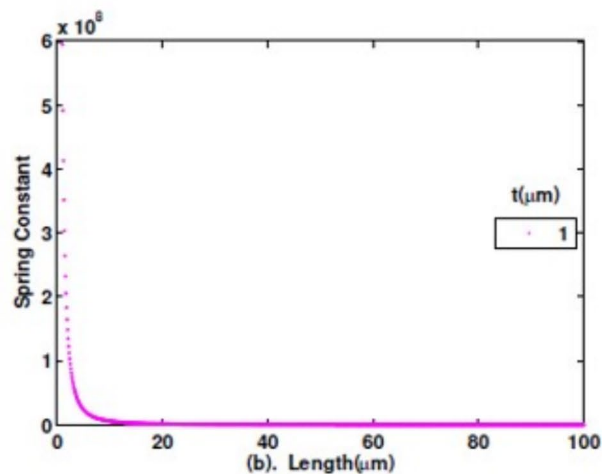

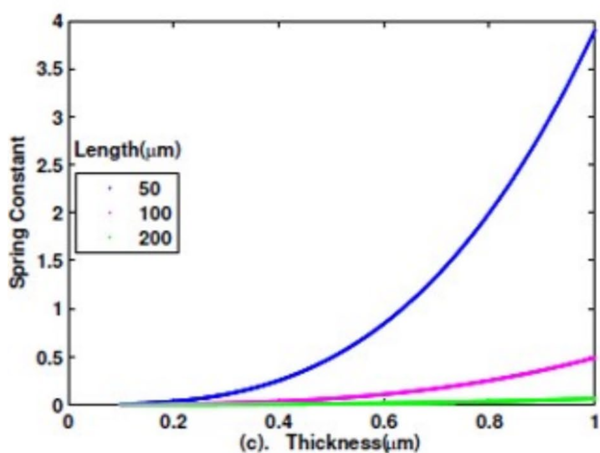

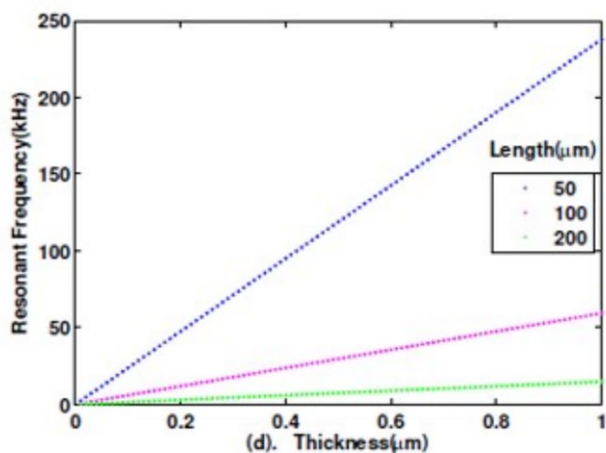

Fig. 15 Variation of "k" and f_0 with respect to physical parameters of MCB

where "D" is the differential-operator, "ω" is displacement in z direction, "ρ" is material-density, "c" is damping-constant, "h" is thickness, and "q" is the applied force on MCB.

$$D(\omega) = EI\frac{\partial}{\partial y^4} \tag{18}$$

where "I" is inertia. For Si material, maximum yield strength is known to be 7000 MPa. The maximum force that is applied on MCB of considered dimensions is calculated using the formula [58].

$$F = \frac{\sigma_b Wh^2}{6L} \tag{19}$$

where "σ_b" is maximum bending stress. The FEM method is used to analyze stress distribution in the complicated mechanical structures. The COMSOL Multiphysics FEM software is used for the stress analysis [59].

The maximum stress on the MCB is expressed as

$$\sigma_b = \frac{6FL}{Wt^2} \tag{20}$$

The maximum stress (according to the Eq. 20) at fixed edge of MCB is optimized at 330 MPa by considering the length, width, and thickness of 75 µm, 15 µm, and 300 nm respectively. This optimized stress on force sensor is almost less than 20 times of the maximum allowable stress on silicon cantilever beam [60].

IO-MEMS MR based force sensor

The schematic of force sensor is illustrated in the Fig. 16. The sensor is the combination of MCB and k MR. In this, microring of MR is integrated on the base of a MCB, and to experience the maximum stress, input-transmission port of MR is integrated at the fixed edge as shown in Fig. 16. The working principle of photo-elastic effect with opto-mechanical coupling. The resonant wavelength shift in transmission spectra of MR depends on change in n_{eff} of input-transmission port. The opto-mechanical characteristics of this force sensor is analyzed in two phases.

Stress analysis of force sensor using FEM

The stress-induced curvature of MCB offers an attractive way to the stress analysis of the surfaces, hence a rectangular MCB in which, one edge is fixed(fixed edge) at one end and the other edge is free (free edge) is considered as a mechanical structure, and an IO microring resonator (MR) which is highly sensitive to any external perturbation is considered as IO sensing element [1, 61].

Generally, the shift in resonant wavelength of the transmission characteristics of IOMEMS device(in this analysis MR) is due to one of following effects or with the combination of the others:

1. The change in local ERI of the waveguide(due to photo-elastic effect)
2. The change in gap or coupling coefficient (due to the displacement)

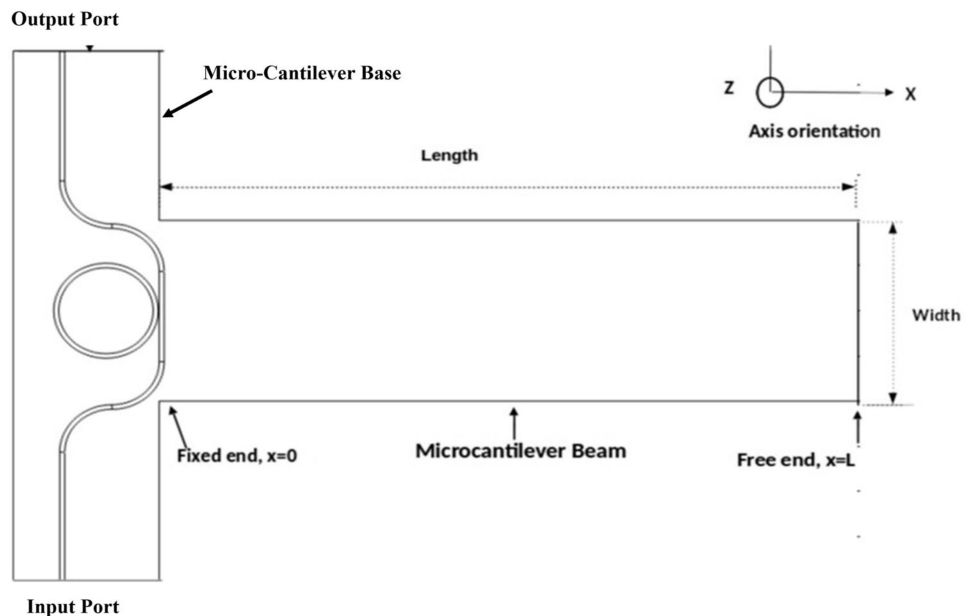

Fig. 16 Schematic of IO-MEMS MR based force sensor

3. The change in dimensions of the device waveguide of the IO MEMS devices (MR) either increase(due to displacement) or decrease(shrinks due to the Poisson's effect).

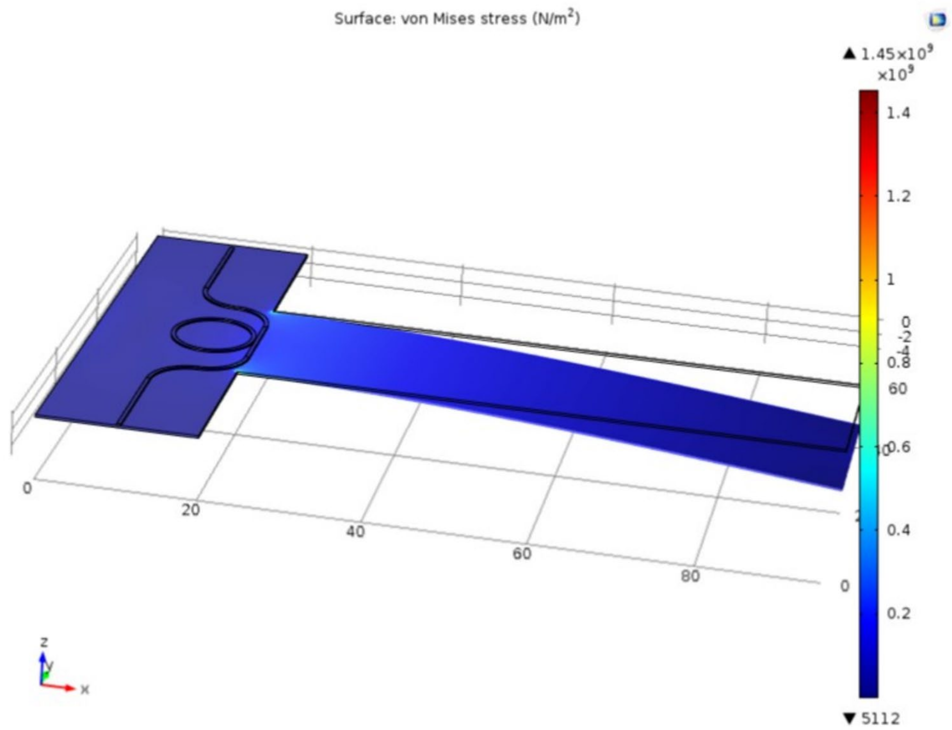

Fig. 17 Stress distribution for a 1 μN force along the MCB's length

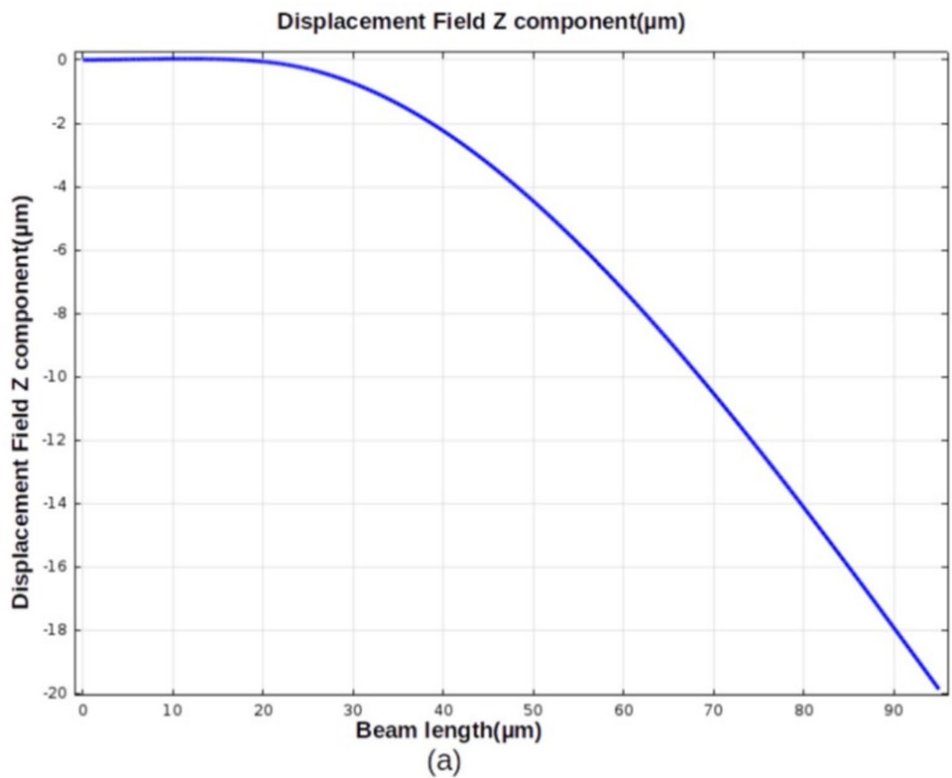

Fig. 18 Displacement variation is linear along MCB for 1 μN force

When force is applied at MCB's free end, it causes a change in coupling-gap in between microring and input-transmission port of MR and which in term change in ERI of input-transmission port. The change in ERI and coupling-gap leads a shift in resonant wavelength of of force sensor's MR.

The stress distribution of force sensor for 1 μN force is as shown in Fig. 17. It is observed that the maximum displacement is 20 μm at the free end as shown in the Fig. 18. Due to this displacement, the non linear stress distribution along the length of MCB is illustrated in Fig. 19.

According to the Eq. 20, the stress is inversely proportional to the thickness and due to the integration of waveguide of MR, the thickness varies at the base of MCB, it is 520 nm i.e., thickness of MR is 220 nm and MCB is 300 nm. Hence, the stress variation is non linear due to the variation of the thickness in the micro cantilever. It is observed from Fig. 19 that the maximum stress is 200 MPa at the fixed edge but it decays linearly along the beam towards the free end. Hence, the transmission port is integrated at the base of MCB.

Optomechanical coupling

Due to opto mechanical coupling, for the applied force at free end of MCB, MCB deforms from equilibrium state and simultaneously there is a stress distribution along the MCB as illustrated in Fig. 17. The stress is maximum at the fixed edge. In turn, this stress changes the local n_{eff} of input, transmission port and also changes the coupling-gap in between microring and input-transmission port of MR. The phase change due to opto-mechanical coupling is given by

$$\Delta\phi = \frac{2\pi}{\lambda}\Delta n_{eff} W \tag{21}$$

where "W" is the input-transmission port width of MR. From equation it is observed that the maximum $\Delta\phi$ depends on maximum width of the waveguide. Due to opto-mechanical coupling, a change in local $n_{e}ff$, changes the phase, correspondingly there is a shift in resonant wavelength of output characteristics of MR.

The change in resonant wavelength is given by

$$\Delta\lambda = FSR\frac{\Delta\phi}{2\pi} \tag{22}$$

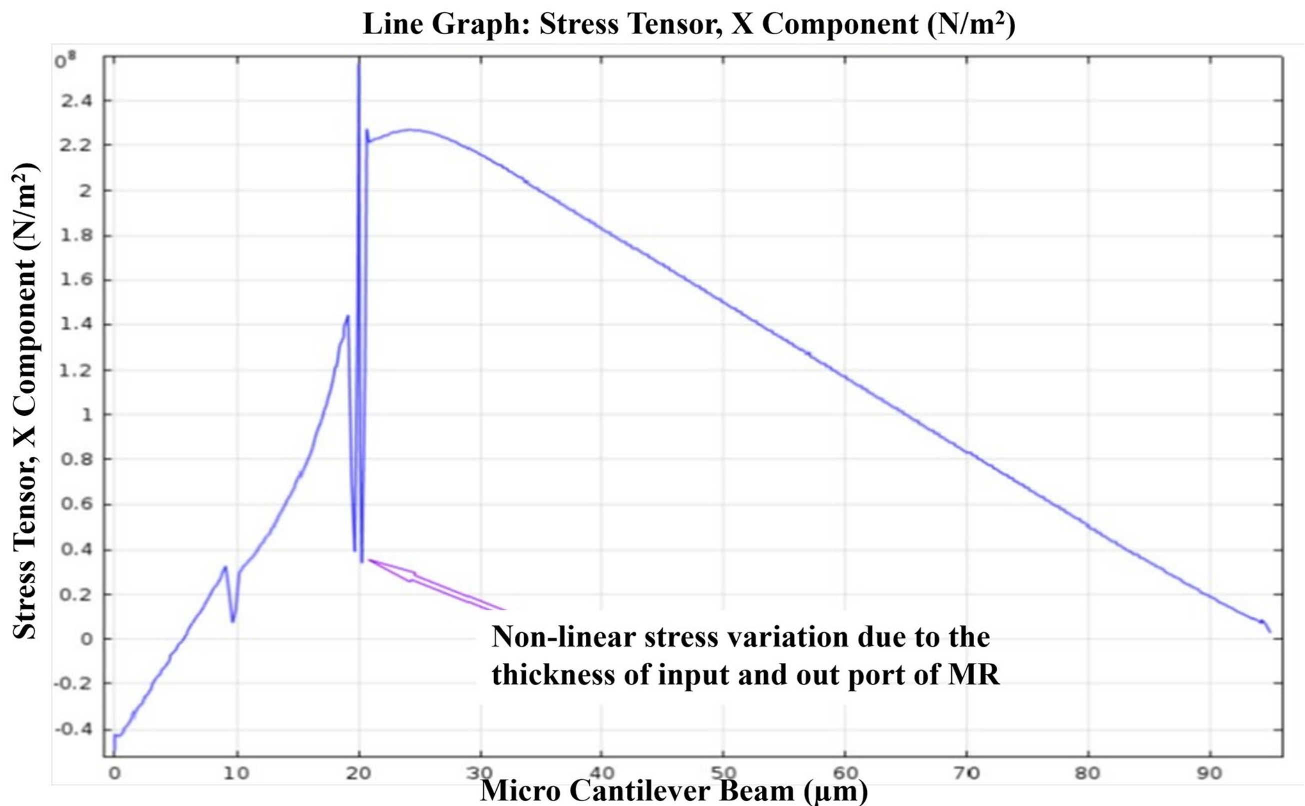

Fig. 19 Non linear variation of Stress along the MCB's length for 1 μN force

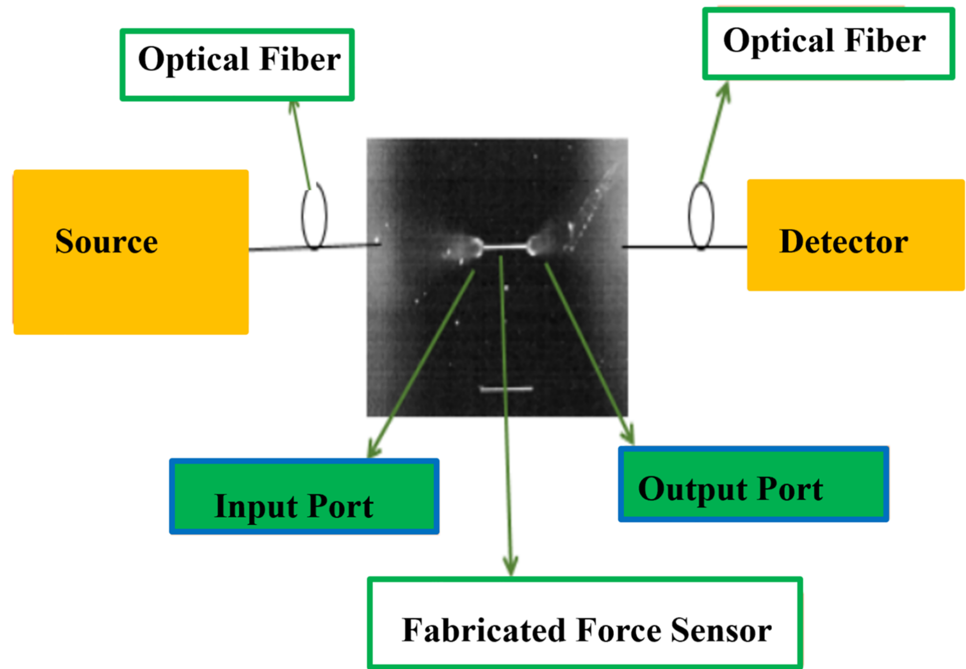

Fig. 20 Block Diagram of Experimental Set-up

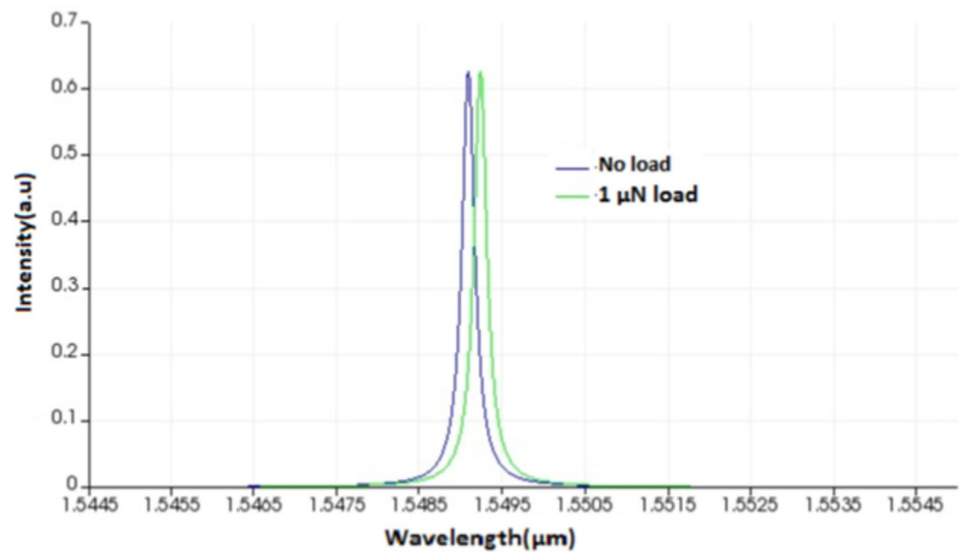

Fig. 21 Transmission spectra of Force Sensor at 0 μN and 1 μN Force

From Eq. 22, it is observed that higher sensitivity depends on FSR and phase shift. The FSR remains constant but the high phase shift depends on the maximum change in n_{eff} (Eq. 21).

Characteristics of force sensor

The experimental configuration utilized to characterize the MR is displayed in Fig. 20. The input-grating receives source, which is coupled into the force sensor. The optical spectrum analyzer is used to view the output. Any change in the applied force can be observed as a change in the resonant wavelength of force sensor [62].

Table 5 Comparison of different force sensors

IO sensing element	FSR (nm)	FWHM (nm)	Q-factor	Sensitivity
MR [This sensor]	29.29	0.09	18,241	5 pm
RTR [48]	17.93	0.19	8153	120 pm
SCMR [49]	114	0.08	21,514	0.34 nm

The sensitivity is defined as the ratio of a change in resonant wavelength $\triangle\lambda_o$ to the change in force $\triangle F$.

$$S = \frac{\triangle\lambda_o}{\triangle F} \tag{23}$$

Figure 21 illustrates the resonant wavelength shift from no load to 1 μN load.

Comparison of different force sensors

Table 5 depicts the comparison of force sensors based on microring resonator (MR), Racetrackring Resonator (RTR), Serially coupled Microring Resonator (SCMR). When comparing three sensors, SCMR based force sensor provides high Q-factor and sensitivity compared to other sensors. RTR based force sensor provides less Q-factor and high sensitivity compared to MR based force sensor. But MR based force sensor provieds high Q-factor with less sensitivity. The less sensitivity is due to the less interaction length of microring and bus waveguide of MR.

Conclusion

The optimized MR and MR based force sensor is reported. The coupling gap, bus waveguide's width and microring's width of MR is optimized using the FDTD Method. The coupling gap in between 150 nm to 200 nm, the microring's width of 500 nm and the bus waveguide's width of 450 nm are considered as an optimized parameters of MR The radius and thickness of MR is considered as 5 μm and 220 nm respectively, and length, width and thickness of MCB is considered as 75 μm, 15 μm and 300 nm respectively. The optimized MR provides, Q-factor of 7590 and FSR of 22.29 nm. The sensitivity of the force sensor is 5 pm per 1 μN. The sensor range from is 0 to 1 μN. The high Q-factor of 18,241 is achieved at the MR's coupling-gap of 200 nm. This MR can be used for different sensing applications such as force, pressure, acceleration sensing, bio sensing and other various sensing applications.

Future work: Fabrication of highly sensitive devices and characterization of the same.

References

1. H. Tai-Ran, MEMS & MICROSYSTEMS, in *Design and Manufacture*. (McGraw-Hill Inc, New York, 2002), pp.112–116
2. D. Rugar, H.J. Mamin, P. Guethner, Improved fiber-optic interferometer for atomic force microscopy. Appl. Phys. Lett. **55**, 2588–2590 (1989)
3. G. Binnig, C.F. Quate, Ch. Gerber, Atomic force microscope. Phys. Rev. Lett. **56**, 930–933 (1986)
4. S. Akamine, T.R. Albrecht, M.J. Zdeblick, C.F. Quate, Microfabricated scanning tunneling microscope. IEEE Electron Device Lett. **10**, 490–492 (1989)
5. M. Tortonese, H. Yamada, R.C. Barrett, C.F. Quate, Atomic force microscopy using a piezoresistive cantilever, in *TRANSDUCERS'91: 1991 International Conference on Solid-State Sensors and Actuators. Digest of Technical Papers* (1991)
6. S.R. Manalis, S.C. Minne, A. Atalar, C.F. Quate, Interdigital cantilever for atomic force microscopy. Appl. Phys. Lett. **69**, 3944–3946 (1996)
7. R.V. Jones, Atomic Force Microscopy, Proc. IEEE **17**, 1185 (1970)
8. A. Niehusmann, P.H. Vorckel, T. Bolivar, W. Wahlbrink, H. Kurz. Henschel, Ultrahigh-quality-factor silicon-on-insulator micro ring resonator. Opt. Lett. **29**(24), 2861–2863 (2004)
9. T. Tsuchizawa, K. Yamada, H. Fukuda, T. Watanabe, J.I. Takahashi, M. Takahashi, T. Shoji, E. Tamechika, S.I. Itabashi, H. Morita, Microphotonics devices based on silicon microfabrication technology. IEEE JSTQE **11**, 232–240 (2005)
10. I. Kiyat, A. Aydinli, N. Dagli, High-Q silicon-on-insulator optical rib waveguide racetrack resonators. Opt. Express **13**(6), 1900–1905 (2005)
11. S. Mookherjea, A. Melloni, Microring resonators in integrated optics (2008)
12. N. Hodgson, H. Weber, *Optical Resonators* (Springer-Verlag, Berlin, 1997)
13. D. Marcuse, *Light Transmission Optics* (Van Nostrand, New York, 1972)
14. K.J. Vahala, Optical microcavities. Nature **424**, 839–846 (2003)
15. F. Michelotti, A. Driessen, M. Bertolotti, Microresonators as building blocks for VLSI photonics, in *AIP Conference Proceedings* (2004)
16. M. Kohtoku, S. Oku, Y. Kadota, Y. Shibata, Y. Yoshikuni, 200-GHz FSR periodic multi-demultiplexer with flattened transmission and rejection band by using a Mach-Zehnder interferometer with a ring resonator. IEEE Photon. Technol. Lett. **12**, 1174–6 (2000)
17. E.M. Dowling, D.L. MacFarlane, Lightwave lattice filters for optically multiplexed communication systems. J. Lightwave Technol. **12**, 471–486 (1994)
18. B.E. Little, H.A. Haus, J.S. Foresi, L.C. Kimerling, E.P. Ippen, D.J. Ripin, Wavelength switching and routing using absorption and resonance. IEEE Photon. Technol. Lett. **10**, 816–918 (1998)
19. J.M. Choi, R.K. Lee, A. Yariv, Control of critical coupling in a ring resonator-fiber configuration: application to wavelength-selective switching, modulation, amplification, and oscillation. Opt. Lett. **26**, 1236–8 (2001)
20. O. Schwelb, Transmission, group delay, and dispersion in single-ring optical resonators and add/drop filters. J. Lightwave Technol. **22**(5), 1380 (2004)
21. S.T. Chu et al., An eight-channel add/drop filter using vertically coupled microring resonator over a cross rid. IEEE Photon. Technol. Lett. **11**, 691–693 (1999)
22. M. Cai, G. Hunzike, K. Vahala, Fiber-optic add-drop device based on a silica microsphere whispering gallery mode system. IEEE Photon. Technol. Lett. **11**, 686–687 (1999)
23. J. Capmany, J. Cascón, Discrete time fiber-optic signal processors using optical amplifiers. J. Lightwave Technol. **12**, 106–117 (1994)
24. C.K. Madsen, J.H. Zhao, *Optical Filter Design and Analysis: A Signal Processing Approach* (Wiley, New York, 1999)
25. S. Tai, K. Kyuma, K. Hamanaka, T. Nakayama, Applications of fiber optic ring resonators using laser diodes. Opt. Acta **33**(12), 1539–1551 (1986)

26. B. Liu, A. Shakouri, J.E. Bowers, Wide tunable double ring resonator coupled lasers. IEEE Photon. Technol. **14**(5), 600–602 (2002)
27. S.M. Spillane, T.J. Kippenberg, K.J. Vahala, Ultralow threshold Raman laser using a spherical dielectric microcavity. Nature **415**, 621–623 (2002)
28. W. Bogaerts, P. De Heyn, T. Van Vaerenbergh, K. De Vos, S. Kumar Selvaraja, T. Claes, P. Dumon, P. Bienstman, D. Van Thourhout, R. Baets, Silicon microring resonators. Laser Photonics Rev. **6**(1), 47–73 (2012)
29. R.V. Kruzelecky et al., Advanced MEMS and integrated-optic components for multifunctional integrated optical micromachines, in *2004 International Conference on MEMS, NANO and Smart Systems (ICMENS'04), Banff, AB, Canada* (2004), pp. 315-321
30. K.D. Vos, I. Bartolozzi, E. Schacht, P. Bienstman, R. Baets, Silicon-on-insulator microring resonator for sensitive and label-free biosensing. Opt. Express **15**(12), 7610–7615 (2007)
31. R. Ozalia, P. Lützow, J. Burgmeier, J. Koch, H. Heidrich, W. Schade, N. Welschoff, S. Waldvogel, A microring resonator sensor for sensitive detection of 1, 3, 5-trinitrotoluene (TNT). Sensors **10**(7), 6788–6795 (2010)
32. A. Haddadpour, Y. Yi, Metallic nanoparticle on micro ring resonator for bio optical detection and sensing. Biomed. Opt. Express **1**(2), 378–384 (2010)
33. R.W. Boyd, J.E. Heebner, Sensitive disk resonator photonic biosensor. Appl. Opt. **40**, 5742–5747 (2001)
34. C.Y. Chao, L.J. Guo, Biochemical sensors based on polymer microrings with sharp asymmetrical resonance. Appl. Phys. Lett. **83**, 1527–1529 (2003)
35. C. Hou, Y. Wu, X. Zeng, S. Zhao, Q. Zhou, G. Yang, Novel high sensitivity accelerometer based on a microfiber loop resonator. Opt. Eng. **49**(1), 014402 (2010)
36. N.C. Loh, M.A. Schmidt, S.R. Manalis, Sub-10 cm/sup 3/ interferometric accelerometer with nano-g resolution. J. Microelectromech. Syst. **11**(3), 182–187 (2002)
37. M. Okhawa, M. Izutsu, T. Sueta, Integrated optical accelerometer employing a cantilever on a silicon substrate. Jpn. J. Appl. Phys. **28**(2), 287–288 (1989)
38. Storgaard K.E.. Burcham, G.N. De Brabender, J.T. Boyd, Micromachined silicon cantilever beam accelerometer incorporating an integrated optical waveguide. Proc. SPIE **1793**, 12–18 (1992)
39. W. Mo, H. Wu, D. Gao, Z. Zhou, Analysis of silicon-based optical racetrack resonator for acceleration sensing, in *Proceedings of SPIE* (2010)
40. P.K. Pattnaik, Analysis and design of micro-opto-electro-mechanical systems (MOEMS), based pressure and vibration sensors, Department of Electrical Communication Engineering, Indian Institute of Science, Bangalore (2005)
41. S.M.C. Abdulla, L.J. Kauppinen, M. Dijkstra, M.J. de Boer, E. Berenschot, H.V. Jansen, R.M. de Ridder, G.J.M. Krijnen, Tuning a racetrack ring resonator by an integrated dielectric MEMS cantilever. Opt. Express **19**(17), 15864–15878 (2011)
42. S.M. Sherif, M.Y. Elsayed, L.A. Shahada, M.A. Swillam, Vertical silicon nanowire-based racetrack resonator optical sensor. Appl. Phys. A **125**, 769 (2019)
43. M.M. Ariannejad, E. Akbari, M. Niazi, E. Hanafi, Urea sensor by racetrack silicon resonator. Optik **208**, 164042 (2020)
44. I. Kiyat, C. Kocabas, A. Aydinli, Integrated micro ring resonator displacement sensor for scanning probe microscopies. Micromech. Microeng. **14**, 374–381 (2004)
45. X. Liu, C. Xue, S. Van, J. Xiong, W. Zhang, Integrated high sensitivity displacement sensor based on micro ring resonator. J. Micromech. Microeng. **14**, 374–381 (2004)
46. M. Tortonese, Cantilevers and tips for atomic force microscopy. IEEE Eng. Med. Biol. **16**(2), 28–33 (1997)
47. S.R. Manalis et al., Interdigital cantilever for atomic force microscopy. Appl. Phys. Lett. **69**(25), 3944–3946 (1996)
48. V.R. Kolli, S. Talabattula, Design and analysis of MEMS racetrack resonators for force sensing applications, in *IEEE CONECCT* (2020)
49. V.R. Kolli et al., Design and analysis of serially coupled double microring resonator based force sensor for 1 μN range measurement. Optik **131**, 1063–1070 (2017)
50. V.R. Kolli, R. Chaparala, S. Tupakula, S. Talabattula, A highly sensitive integrated optic serially coupled racetrack ring resonator based pressure sensor. Opt. Mater. **149**, 115018 (2024)
51. D.G. Rabus, *Integrated Ring Resonators* (Springer, Berlin, 2007), pp.3–40
52. V.R. Kolli, S. Talabattula, An optimized integrated optical coupled micro ring resonator for low pressure sensing. IEEE Sens. J. **22**(16), 16016–16026 (2022)
53. O. Powell, Single-mode condition for silicon RIB waveguides. J. Lightwave Technol. **20**, 1851 (2002)
54. J. Lousteau, D. Furniss, A. Seddon, T.M. Benson, A. Vukovic, P. Sewell, The single-mode condition for silicon-on-insulator optical RIB waveguides with large cross section. J. Lightwave Technol. **22**, 1923 (2004)
55. M.A. Hopcroft, W.D. Nix, T.W. Kenny, What is the Youngs modulus of silicon. J. Microelectromech. Syst. **19**(2), 229–238 (2010)
56. J. Marty, A. Malki, C. Renouf, P. Lecoy, F. Baillieu, Fibber optic accelerometer using silicon micromachining techniques. Sens. Actuators Phys. A **46–47**, 470–473 (1995)
57. W. Soedel, *Vibration of Shells and Plates* (Marcel Dekker Inc., New York, 1993)
58. B. Bhola, W.H. Steier, A novel optical microring resonator accelerometer. IEEE Sens. J. **7**(12), 1759–1766 (2007)
59. http://www.comsol.com/
60. K.E. Peterson, Silicon as a mechanical material. Proc. IEEE **70**(5), 420–457 (1982)
61. R.V. Kruzelecky, B. Wong, J. Zou, E. Haddad, W. Jamroz, A. Yelon, R. Beaudry, O. Grenier, W. Zheng, L.N. Phong, Advanced MEMS and integrated-optic components for multifunctional integrated optical micromachines, in *2004 International Conference on MEMS, NANO and Smart Systems (ICMENS'04)* (2004), pp. 315–321
62. V.R. Kolli, T.R. Yadunath, R.K. Resmi, G. Hegde, T. Badrinarayana, P.P. Das, T. Srinivas, Design, fabrication and characterization of 5 μm ring resonator, in *International Conference on Fibre Optics and Photonics* (2016)

Publisher's Note Springer Nature remains neutral with regard to jurisdictional claims in published maps and institutional affiliations.

Springer Nature or its licensor (e.g. a society or other partner) holds exclusive rights to this article under a publishing agreement with the author(s) or other rightsholder(s); author self-archiving of the accepted manuscript version of this article is solely governed by the terms of such publishing agreement and applicable law.